PHYSICAL REVIEW D

PARTICLES AND FIELDS

THIRD SERIES, VOLUME 25, NUMBER 1 1 JANUARY 1982

Measurement of quark momentum distributions in the proton using an antineutrino probe

V. E. Barnes, T. S. Carman, D. D. Carmony, E. Fernandez,* A. F. Garfinkel, and A. T. Laasanen
Purdue University, West Lafayette, Indiana 47907

M. Derrick, P. Gregory,† F. LoPinto,‡ B. Musgrave, J. Schlereth, P. Schreiner,‡ and R. Singer‡
Argonne National Laboratory, Argonne, Illinois 60439

S. J. Barish§, R. Brock,|| A. Engler, T. Kikuchi, R. W. Kraemer, F. Messing, B. J. Stacey,¶ and M. Tabak**
Carnegie-Mellon University, Pittsburgh, Pennsylvania 15213

(Received 19 June 1981)

We present the results of a study of the inclusive reaction $\bar{\nu}p \to \mu^+ X^0$ for antineutrino energies from 5 to 150 GeV. The data were obtained by exposing the Fermi National Accelerator Laboratory hydrogen-filled 15-foot bubble chamber to a wide-band antineutrino beam. This is the first high-energy antineutrino experiment in which a pure proton target was used. The experimental problems of selecting the required sample of charged-current antineutrino-induced events are discussed in detail. A Monte Carlo simulation of the experiment is used to provide correction factors to the measured distributions. A measurement of the x dependence of the inelasticity (y) distributions gives the proton structure functions $F_2^{\bar{\nu}p}(x)$ and $xF_3^{\bar{\nu}p}(x)$ up to an overall normalization constant. When expressed in terms of the quark-parton model, the quark distributions $u(x)$ and $\bar{d}(x)+\bar{s}(x)$ are determined. The results for $u(x)$ are found to be in excellent agreement with models based on fits to electron and muon scattering data. Using these results to fix the $u(x)$ normalization, an absolute measurement is made of $x[\bar{d}(x)+\bar{s}(x)]$, the antiquark momentum distribution.

I. INTRODUCTION

Lepton-nucleon scattering experiments are a particularly good way to study the structure of the nucleon. In the quark-parton model[1] (QPM), the collision process is described as the incoherent scattering of the incoming lepton from one of the quarks in the target and, as shown below, the inclusive lepton-nucleon cross section can be used to extract information about the quark momentum distribution inside the nucleon. Neutrino and antineutrino probes are of particular interest, since the chiral nature of the weak current allows a separation of the quark and antiquark contributions to the scattering.

In general, the inclusive charged-current (CC) processes

$$\nu N \to \mu^- + \text{anything}\ , \tag{1}$$

$$\bar{\nu}N \to \mu^+ + \text{anything} \tag{2}$$

are phenomenologically described by the diagrams of Fig. 1. The incoming neutrino changes to a charged lepton at the leptonic vertex and transfers momentum to the nucleon through the exchange of a virtual intermediate vector boson. For a given neutrino energy E_ν, there are only two independent kinematical variables, and these can be chosen as the Bjorken scaling variables x and y defined by

$$x = \frac{Q^2}{2M\nu}\ , \tag{3}$$

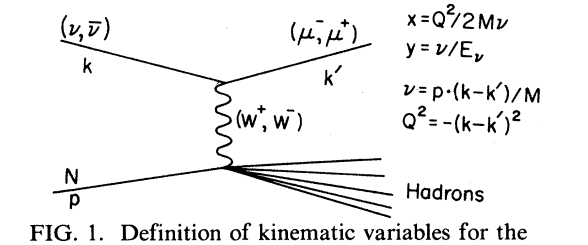

FIG. 1. Definition of kinematic variables for the reaction $\nu N \to \mu +$ anything.

$$y=\frac{\nu}{E_\nu}\ , \tag{4}$$

where $Q^2=-(k-k')^2$ is the four-momentum transfer and $\nu=p\cdot(k-k')/M=E_\nu-E_\mu$ is the so-called energy transfer. In these equations, k and k' are the four-momenta of the neutrino and muon, respectively. The nucleon is defined by its four-momentum p and mass M, and E_ν and E_μ are, respectively, the laboratory energies of the neutrino and the muon. From the kinematics, one can see that x and y are bounded by 0 and 1.

Assuming that the interaction is of the current-current form (which is equivalent to neglecting propagator effects in the diagram of Fig. 1) and that the current at the leptonic vertex has the usual $V-A$ structure, the cross section for the inclusive processes (1) and (2) can be written as[4]

$$\frac{d^2\sigma}{dx\,dy}=\frac{G^2ME_\nu}{\pi}\left[\left(1-y-\frac{Mxy}{2E_\nu}\right)F_2(x,Q^2)+xy^2F_1(x,Q^2)\pm y\left(1-\frac{y}{2}\right)xF_3(x,Q^2)\right]\ , \tag{5}$$

where the upper and lower signs refer to the neutrino and antineutrino reactions, respectively. At high energy, the term $Mxy/2E_\nu$ is negligible compared to unity and we can write Eq. (5) as

$$\frac{d^2\sigma}{dx\,dy}=\frac{G^2ME_\nu}{2\pi}[(2xF_1\pm xF_3)+(2xF_1\mp xF_3)(1-y)^2+2(F_2-2xF_1)(1-y)]. \tag{6}$$

There are then four different sets of the three structure functions $F_i(x,Q^2)$ corresponding to the use of ν or $\bar{\nu}$ particles as projectiles incident on neutron or proton targets.

In early electron[2] and neutrino[3] scattering experiments, it was observed that within the experimental uncertainties, the structure functions for fixed x were independent of Q^2. This property, known as scaling, had been predicted by Bjorken[4] for the deep-inelastic region of large ν and Q^2. If scaling holds, the total neutrino charged-current cross section becomes proportional to the energy E_ν, and the x and y distributions are independent of E_ν. The proportionality of cross section to neutrino energy is found experimentally to hold down to $E_\nu\sim 1$ GeV.[5]

The QPM offers a simple understanding of this scaling behavior of the structure functions. In this model the nucleon is considered to be a bound state of pointlike constituents called partons. The partons are further identified with the fractionally charged spin-$\frac{1}{2}$ quarks, and the weak interactions of the quarks are assumed to be identical to the weak interactions of the leptons. In the so-called naive QPM in which scaling is exact and the quarks behave as if they are free during the collision, the transverse momentum of the quarks within the nucleon is neglected. As a consequence of the spin-$\frac{1}{2}$ nature of the quarks, the relationship known as the Callan-Gross relation,[6] $2xF_1=F_2$, holds. In this case, the last term in Eq. (6) is zero.

The variable x is identified in the model with the fraction of the nucleon momentum carried by the struck quark,[1] and the structure functions $F_2(x)$ and $xF_3(x)$ are simple combinations of quark and antiquark momentum distributions. In the case of a proton target, they are

$$F_2^{\nu p}(x)=2x[d(x)+\bar{u}(x)+s(x)]\ , \tag{7}$$

$$xF_3^{\nu p}(x)=2x[d(x)-\bar{u}(x)+s(x)]\ ,$$

$$F_2^{\bar{\nu}p}(x)=2x[u(x)+\bar{d}(x)+\bar{s}(x)]\ , \tag{8}$$

$$xF_3^{\bar{\nu}p}(x)=2x[u(x)-\bar{d}(x)-\bar{s}(x)]\ ,$$

where the quark momentum distributions $u(x)$, $d(x)$, $s(x)$ and the corresponding antiquark momentum distributions $\bar{u}(x)$, $\bar{d}(x)$, $\bar{s}(x)$ refer specifically to the proton. In these equations, we have neglected the contributions from charm and other heavier quarks. These effects are expected to be very small at our energies due to the high masses of the charm and bottom quarks. We have also assumed that all threshold effects are saturated. Equation (6) can then be written in the exact Callan-Gross limit as

$$\frac{d^2\sigma^{\nu p}}{dx\,dy}=\frac{G^2ME}{\pi}2x[d(x)+s(x)+(1-y)^2\bar{u}(x)]\ , \tag{9}$$

$$\frac{d^2\sigma^{\bar{\nu}p}}{dx\,dy}=\frac{G^2ME}{\pi}2x[\bar{d}(x)+\bar{s}(x)+(1-y)^2u(x)]\ . \tag{10}$$

It is clear from these equations that the study of the inclusive νp and $\bar{\nu}p$ cross sections measures specific quark combinations in the proton.

The combinations in Eq. (10) are unique to $\bar{\nu}p$ scattering.[7] In particular, the coefficient of the term $(1-y)^2$ measures $u(x)$ directly. In contrast, for an isoscalar target, the quark contributions always appear as a $(u+d)$ combination.[8] In electron

and muon scattering experiments, the quark contributions appear as $q+\bar{q}$, with q equal to the sum of the u, d, and s quark distributions, weighted by the square of the quark charge, and in hadron-induced dilepton production experiments, the contribution is in the form of the product $q\bar{q}$.

Clear deviations from scaling have been measured in electron, muon, and neutrino experiments and quantitatively compared to predictions of asymptotically free gauge theories.[9,10] The deviations from scaling are small and require the analysis of data over a large range of Q^2 (or E_ν). The mean Q^2 of our events, $\langle Q^2 \rangle$, is 4.5 $(\mathrm{GeV}/c)^2$, although the tail of the distribution extends beyond 20 $(\mathrm{GeV}/c)^2$. However, most of our events are at moderately low Q^2, and so the experiment lacks sensitivity to the scale breaking seen in other experiments. Small violations of the Callan-Gross relation have also been reported,[9,11] although the experimental situation is far from clear.[12] We also do not make a significant test of the validity of this relation with our data.

In this paper we describe our experimental study of the $\bar{\nu}p$ inclusive cross section. We give the experimental details of the analysis, the principal results of which have been reported previously.[7] The paper is organized as follows. Section II deals with the experimental details. Section III explains our method of extracting the structure functions, and Sec. IV gives the results of our analysis. Finally, in the Appendix, we describe the methods used to select the muon track, to calculate the neutrino energy, and to make the small radiative corrections. In the Appendix we also discuss the Monte Carlo (MC) simulation of the experiment which was used to correct the data for the experimental cuts and for the resolution smearing.

II. EXPERIMENTAL DETAILS

The data sample was obtained from three different exposures of the hydrogen-filled 15-foot bubble chamber to a broad-band antineutrino beam at Fermilab. To produce this beam, an extracted proton beam from the proton synchrotron was focused onto an aluminum target. Negative (positive) particles produced in the target were then focused (defocused) by a pulsed magnetic horn system and allowed to decay in a 340-m-long decay pipe. The bubble chamber is situated approximately 1 km downstream of the end of this pipe. Table I gives the number of pictures taken, the energy and intensity of the extracted proton beam, and the number of stages of the magnetic horn system for each run. The resulting beam has a substantial neutrino background due mainly to positive secondaries which are produced within the opening angle of the horns are, therefore, not defocused. The shapes and relative intensities of the ν and $\bar{\nu}$ fluxes are shown in Fig. 2. The fluxes are calculated using our measured ν- and $\bar{\nu}$-event energy distributions and assuming a linear cross section rise with E_ν. At low energy, these fluxes are clearly larger than those obtained using the Stefanski and White[13] or Wang[14] parametrization of hadron production in aluminum. The discrepancy results from the secondary interactions in the target which are not considered in the simple production models. The units in Fig. 2 are arbitrary since there are large uncertainties in the absolute flux normalizations.

When scanning the film, only events with three or more charged particles were selected. One-prong events were discarded since the scanning efficiency was low due to the large number of single muons traversing the chamber. Events were also rejected at the scanning stage if the total visible momentum in the beam direction (estimated by using a template on the scanning table) was less than 2 GeV/c. This cut eliminates background events caused by incoming hadron tracks which scatter in the chamber as well as a large fraction of the background events caused by low-energy neutrons. In Table II we give the scanning efficiency as a func-

TABLE I. Summary of the experimental runs.

	Number of pictures	Intensity of bubble-chamber magnetic field (kG)	Energy of extracted proton beam (GeV)	Intensity of extracted proton beam (protons per pulse)	Number of magnetic horns
Run 1	24000	21	300	0.6×10^{13}	1
Run 2	38000	30	400	0.8×10^{13}	2
Run 3	146000	30	400	1.4×10^{13}	2

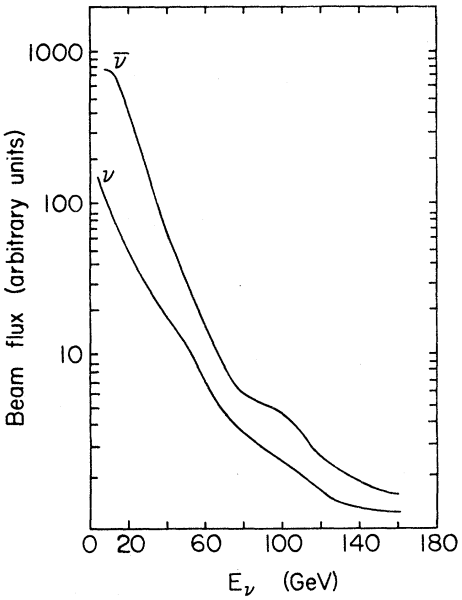

FIG. 2. Shapes and relative intensities of the ν and $\bar{\nu}$ fluxes as determined from the event energy distributions and assuming a linear cross section rise with energy.

tion of topology, calculated from a double scan of more than one-third of the film.

The geometrical reconstruction of the events was made using a modified version of the TVGP program. The fraction of events that are successfully reconstructed, after repeated measurements, is also shown in Table II for the different topologies. Only events inside a fiducial volume of 16.8 m^3, which guarantees a minimum measurable track length of 45 cm, were kept in the sample. Figure 3 shows a scatter plot of $\Delta p/p$ versus p for a sample of tracks. Ninety percent of the hadrons and 80% of the muons have $\Delta p/p < 0.05$. As explained in the Appendix, the momentum resolution is incorporated into the MC program in calculating the smearing corrections.

To completely eliminate the neutron-induced background,[15] events in the sample were required to have more than 5 GeV/c total visible momentum, P_{vis}. To show that this cut is adequate, we interpreted all the three-prong events as $xp \rightarrow pp\pi^-$. A plot of the mass squared of x ($M_x{}^2$) is shown in Fig. 4(a) for the events in the sample.

TABLE II. Scanning and reconstruction efficiencies.

Number of prongs	Scanning efficiency	Geometrical-reconstruction efficiency
$n_{\text{pr}} \leq 3$	0.80	0.94
$4 \leq n_{\text{pr}} \leq 5$	0.93	0.85
$6 \leq n_{\text{pr}} \leq 7$	0.94	0.82
$n_{\text{pr}} > 7$	0.94	0.72

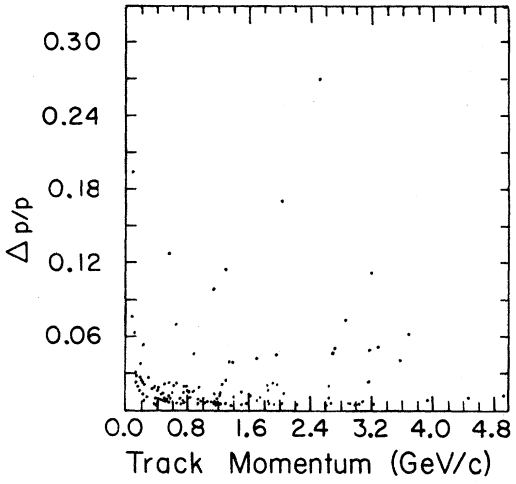

FIG. 3. Scatter plot of $\Delta p/p$ versus track momentum p for a sample of tracks.

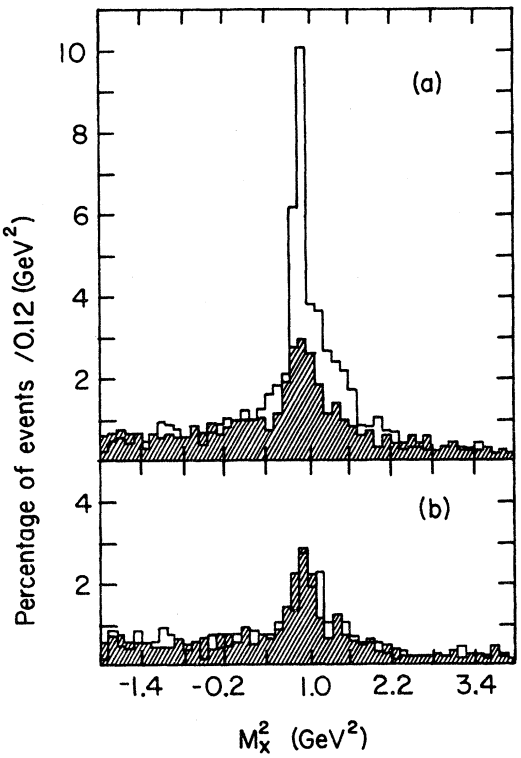

FIG. 4. The open histogram shows the distribution in the square of the beam mass, $M_x{}^2$, for three-prong events interpreted as the reaction $xp \rightarrow pp\pi^-$. (a) All events, (b) events with $P_{\text{vis}} > 5$ GeV/c. The cross-hatched areas show similar distributions for the MC-generated events.

The cross-hatched area is a similar plot for ν and $\bar{\nu}$ MC-generated events normalized to the total number of real events. There is a clear excess of real events at the neutron mass for the low neutrino energies. After the $P_{\rm vis} > 5$ GeV/c cut is imposed, this excess disappears, as is apparent from Fig. 4(b).

After all the above-mentioned cuts, we have 2275 events selected as the charged-current reaction

$$\bar{\nu}p \rightarrow \mu^+ X^0 \,. \tag{11}$$

An analysis of the inclusive $\bar{\nu}p$ scattering, based on the first two exposures listed in Table I, has been previously published.[16] The present results are based on about four times more events, as well as a more detailed understanding of the experimental corrections.

III. METHOD OF ANALYSIS

Under the assumption that inclusive scaling is valid and that the Callan-Gross relation is satisfied, the $\bar{\nu}p$ inclusive charged-current (CC) cross section can be written as

$$\frac{d^2\sigma^{\bar{\nu}p}}{dx\,dy} = \frac{G^2 M E_\nu}{2\pi}\{F_2^{\bar{\nu}p}(x) - xF_3^{\bar{\nu}p}(x) + [F_2^{\bar{\nu}p}(x) + xF_3^{\bar{\nu}p}(x)](1-y)^2\} \tag{12}$$

or equivalently in the QPM as

$$\frac{d^2\sigma^{\bar{\nu}p}}{dx\,dy} = \frac{G^2 M E_\nu}{\pi} 2x[\bar{d}(x) + \bar{s}(x) + (1-y)^2 u(x)] \,. \tag{13}$$

It is clear from these equations that fits to the y distributions at fixed x can separate the contribution of $F_2^{\bar{\nu}p}(x)$ and $xF_3^{\bar{\nu}p}(x)$ or equivalently of $u(x)$ and $\bar{d}(x)+\bar{s}(x)$. This is the method that we use. In order to do this separation, it is not necessary to use the full y range and, in fact, in order to avoid large corrections, we find that it is necessary to restrict the y range used in the fits to values between $y = 0.1$ and an upper limit, which depends on x but which is typically $y \simeq 0.8$. These cuts, of course, imply a loss of statistical precision. The method also requires that the corrections to the data be calculated as a function of both x and y.

We note that in the case of a proton target, the structure functions cannot be extracted using the cross-section-difference technique that is commonly used in experiments using isoscalar targets.[8–10] In the isoscalar case, if differences between $s(x)$ and $c(x)$ are ignored, then $F_2^{\nu N}(x) = F_2^{\bar{\nu}N}(x)$ and $xF_3^{\nu N}(x) = xF_3^{\bar{\nu}N}(x)$, and the structure functions can be extracted from the sum and difference of νN and $\bar{\nu}N$ cross sections, respectively. Since $F_i^{\nu p} \neq F_i^{\bar{\nu}p}$, this technique cannot be used in our case.

We now discuss the measurement of the x and y distributions. Since in addition to the antineutrino CC reaction we have neutral-current (NC) and neutrino-induced events, the first problem is to separate the required $\bar{\nu}p$ CC events. This is done by selecting events with a positive-muon track. The muon selection method is based on the kinematics of the charged-current reaction; namely, that the muon track appears in general as a single fast particle separated from a clustered jet of hadrons. A detailed description of the method is given in the Appendix.

With increasing energy transfer (increasing y), the muon is difficult to distinguish from the hadrons, and consequently the efficiency of the method decreases. The background due to ν-induced and NC events, as well as $\bar{\nu}$-induced events in which the wrong track is selected as the μ^+, therefore increases with y. This increase of background with y is particularly severe at low x. In Fig. 5, we show the efficiency and background as functions of y for different regions of x as calculated using the MC simulation of the experiment.

Once the muon track is selected, there remains the problem of calculating the antineutrino energy. This is done using a kinematical method, also discussed in the Appendix. The basic idea of the method is that the direction of the total hadronic system in the ν-μ plane is such that the sum $(P_\perp^2 + m^2)^{1/2}$ extended over all observed hadrons is minimum. In this expression $P_\perp$ is the transverse momentum of the individual hadron with respect to the total hadron direction and m is its mass. If the direction of the total hadronic system is determined, the energy of the event is known. The overall energy resolution $\Delta E/E$, calculated from the MC events, is given in Fig. 6 for different y intervals.

After the muon track is identified and the energy of the event is known, the x and y variables are readily calculated. The biases introduced by the uncertainties in the energy measurement partially cancel out in the calculation of x and y since the energy affects both numerator and denominator of

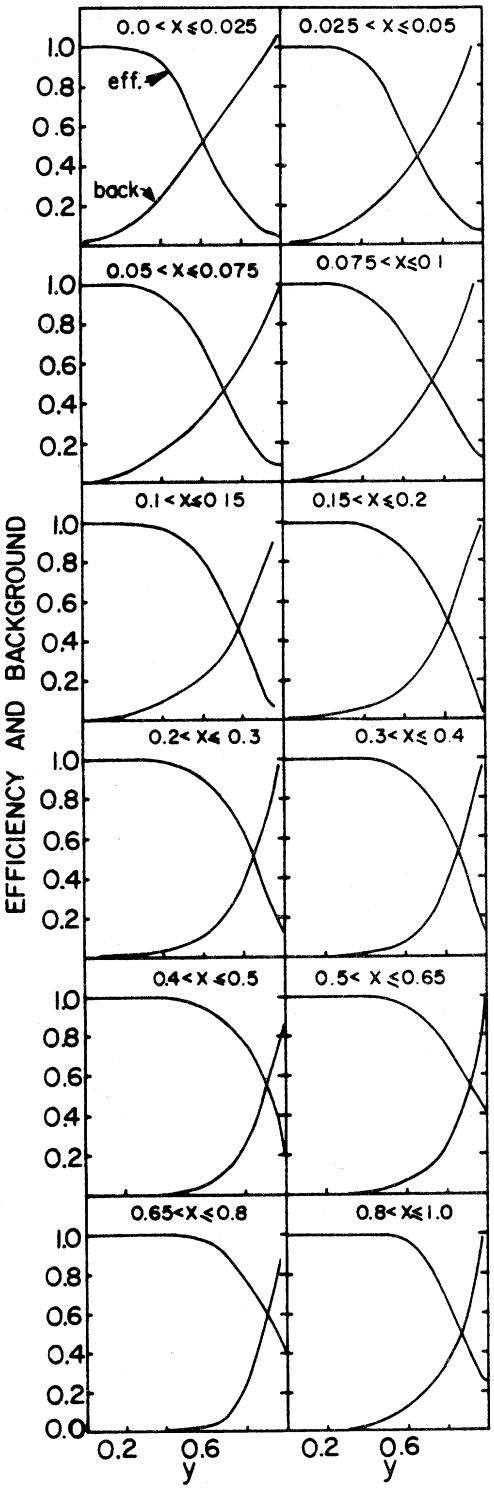

FIG. 5. Efficiencies and backgrounds of the muon selection algorithm as a function of y for different x regions as calculated from the MC-generated events. For all x selections, the efficiency curves fall as y increases.

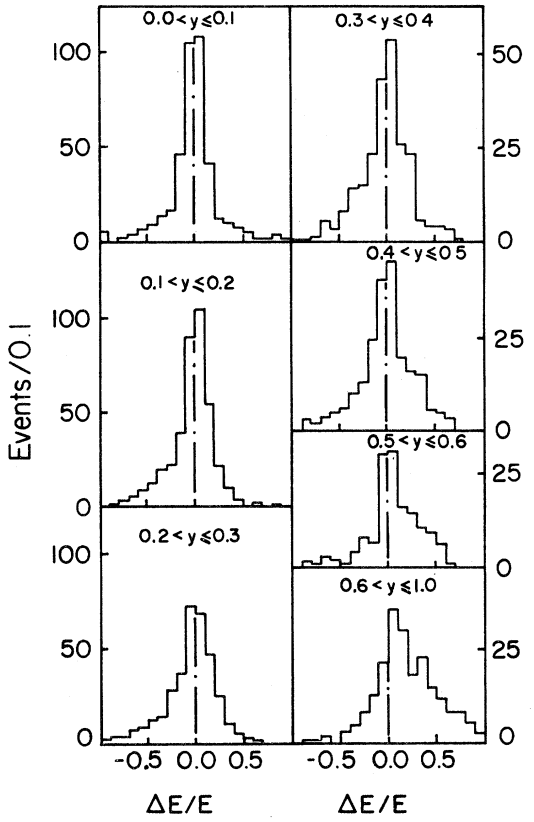

FIG. 6. The distribution in $\Delta E/E$ for different y regions as calculated from the MC events.

Eqs. (3) and (4). The resolutions in x and y, defined as the half-widths at half maximum of the Δx and Δy distributions calculated from the MC events, are given in Table III.

To correct for the biases introduced by the momentum uncertainties on the charged tracks, by the muon selection, and by the energy calculation, as well as for the cuts described in Sec. II, we use a MC simulation of the experiment. A description of the MC program is given in the Appendix. To determine the corrections, the x and y distributions

TABLE III. Resolution in the scaling variables x and y.

	$x \leq 0.3$	$x > 0.3$
$y \leq 0.3$	$\Delta x \sim 0.03$ $\Delta y \sim 0.03$	$\Delta x \sim 0.05$ $\Delta y \sim 0.02$
$y > 0.3$	$\Delta x \sim 0.02$ $\Delta y \sim 0.06$	$\Delta x \sim 0.06$ $\Delta y \sim 0.05$

are calculated from the MC events by treating them as real data. For a given (x,y) bin, we then define the correction factor $C(x,y)$ as

$$C(x,y)=\frac{B(x,y)}{A(x,y)}\ , \tag{14}$$

where $A(x,y)$ is the number of MC events generated in a particular bin of x and y and $B(x,y)$ is the number of events finally populating the same (x,y) bin after all event selections and cuts. The data are corrected by dividing the number of observed events in each (x,y) bin by the value of $C(x,y)$ for this bin. Figure 7 shows the y dependences of the functions $C(x,y)$ for different x intervals, resulting from a sample of 290 000 MC events. The curves are fits to the B/A ratios.

The calculation of the correction factors is an iterative process. We started with a reasonable model as input to the MC and calculated the correction factors. We then used these corrected distributions as input to the MC program. The MC program was continually refined as we measured more details about the structure of the events. The final correction factors are now quite insensitive to variations of the parameters in the program.

It is clear from these figures that there is a loss of events at small y, which is mainly due to the rejection of the one-prong sample. To avoid this large correction, we exclude events with $y<0.1$. The loss of events at high y is due to the inefficiency of the muon selction algorithm. The effect of this inefficiency of the correction factors is partially hidden by the fact that the background introduced by the muon selection method increases with y. As a criterion to determine the upper limit of the y intervals used in the fits, we require that the background at any point be less than 32%. The region of the x-y plane that satisfies this requirement is the region to the left of the curve in Fig. 8. Notice that at small x, the allowed y interval is small, and the background is also changing rapidly so that the results are unreliable. We therefore also exclude the events with $x<0.1$. The region of the x-y plane actually used in the fits is shown in Fig. 8 by the shaded area. The mean background over the x-y region used is 7% and the mean detection efficiency is 97%. After these selections, 1425 events are available for the analysis.

In addition to the experimental corrections, we also include radiative corrections obtained using the calculations of De Rújula *et al.*[17] These corrections, which are described in more detail in the Appendix, are shown in Fig. 9 for a typical energy of 25 GeV. They are very small compared to our statistical errors.

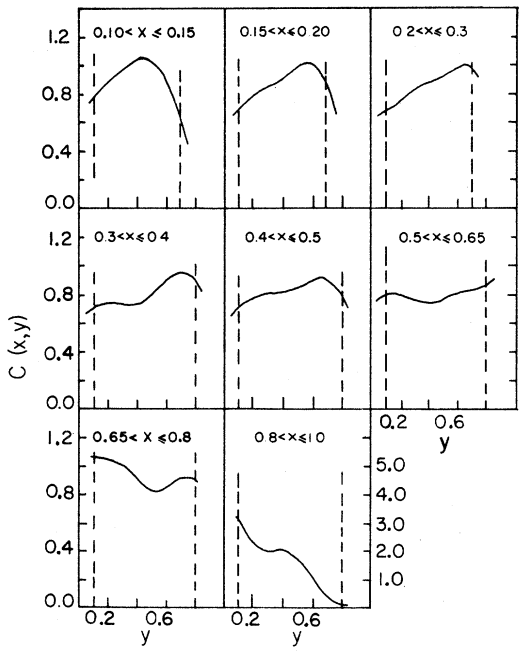

FIG. 7. The y dependence of the correction factors $C(x,y)$ for different regions of x. Only data between the dashed lines are used in the analysis.

IV. RESULTS

Figures 10 and 11 show, respectively, the energy and momentum transfer distributions of the events.

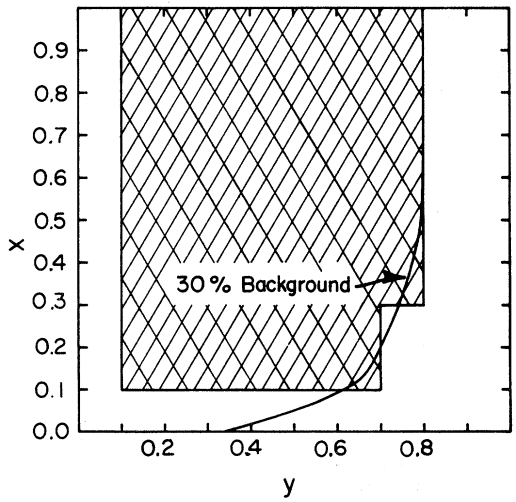

FIG. 8. Region of the x-y plane used in the fits (cross-hatched area). For the region to the left of the curve, the muon-selection background at any point is less than 32%.

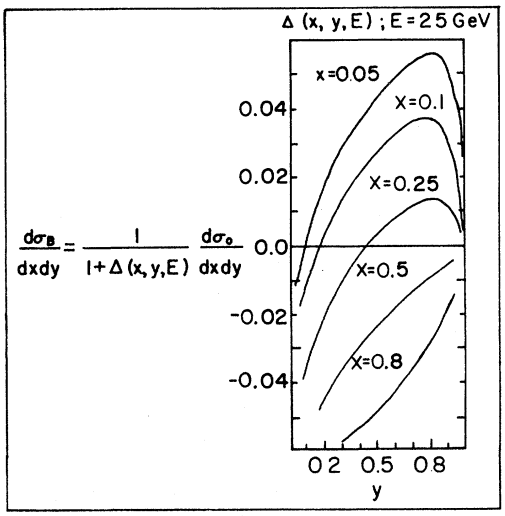

FIG. 9. The calculated radiative corrections shown as a function of y for different x selections for a typical neutrino energy $E_{\bar{\nu}}=25$ GeV. The observed cross section σ_0 is multiplied by the factor $1/[1+\Delta(x,y,E)]$ in order to obtain the true cross section.

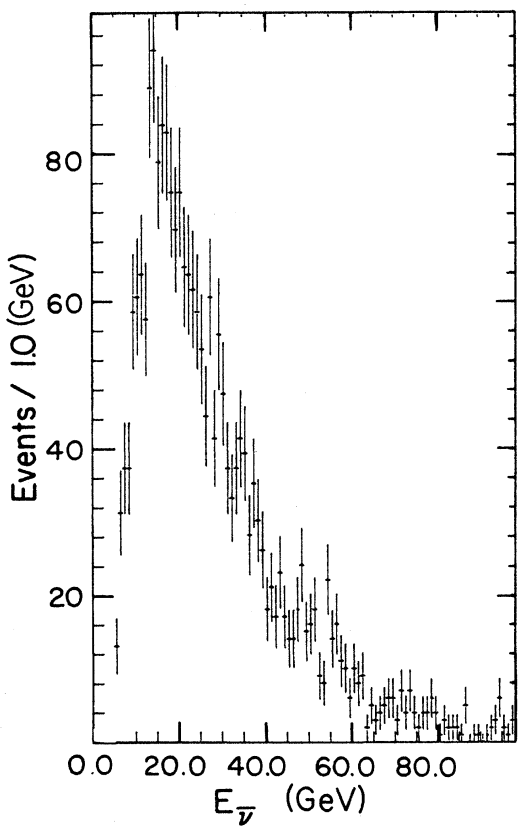

FIG. 10. Observed energy distribution of the antineutrino-induced events.

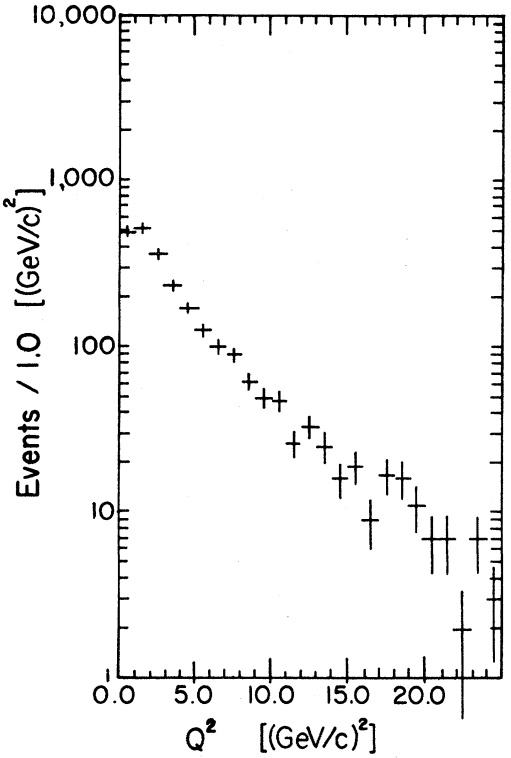

FIG. 11. The observed Q^2 distribution for the antineutrino-induced events.

The average energy and momentum transfer values are $\langle E_{\bar{\nu}}\rangle=31$ GeV, and $\langle Q^2\rangle=4.5$ $(\text{GeV}/c)^2$. In Fig. 12 we show the measured y distributions for different x intervals. To obtain the full distribu-

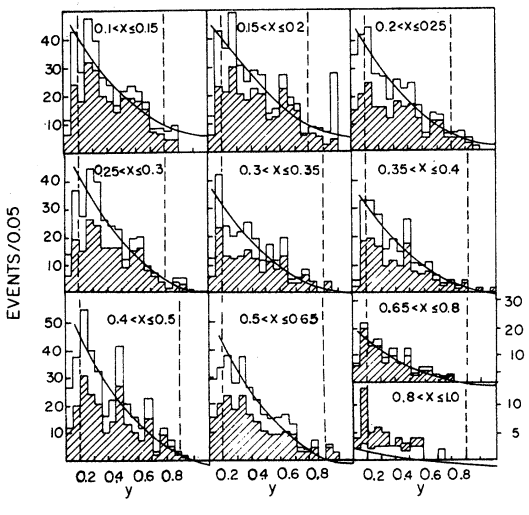

FIG. 12. Fully corrected y distributions for different regions of x. The cross-hatched histogram shows the raw events. The solid curves are fits to the corrected open histograms using the form $a(x)+b(x)(1-y)^2$. The parameter $a(x)$ is not constrained to be positive.

TABLE IV. Results of the y-distribution fits.

x interval	$\langle Q^2 \rangle$ [(GeV/c)^2]	$B(x)$	$b(x)=xu(x)$	$a(x)=x[\bar{d}(x)+\bar{s}(x)]$	$F_2^{\bar{\nu}p}(x)$	$xF_3^{\bar{\nu}p}(x)$	χ^2/DF
(0.10,0.15)	2.2	0.76±0.13	0.58±0.10	0.077±0.037	1.31±0.15	1.00±0.28	1.17
(0.15,0.20)	3.5	0.81±0.12	0.62±0.11	0.066±0.037	1.37±0.16	1.11±0.28	1.47
(0.20,0.25)	3.4	0.87±0.13	0.57±0.11	0.040±0.035	1.23±0.16	1.07±0.27	0.98
(0.25,0.30)	4.4	1.00±0.09	0.70±0.10	0.000±0.030	1.39±0.15	1.39±0.25	1.10
(0.30,0.35)	4.7	1.03±0.06	0.51±0.07	−0.009±0.015	1.01±0.12	1.04±0.16	0.96
(0.35,0.40)	5.0	1.03±0.07	0.50±0.07	−0.008±0.018	0.98±0.12	1.01±0.17	0.68
(0.40,0.50)	6.1	0.98±0.07	0.36±0.05	0.003±0.012	0.72±0.07	0.71±0.11	2.14
(0.50,0.65)	6.5	1.07±0.05	0.23±0.03	−0.007±0.006	0.45±0.04	0.48±0.06	0.58
(0.65,0.80)	7.7	1.12±0.10	0.09±0.02	−0.005±0.004	0.17±0.03	0.19±0.04	0.53
(0.80,1.0)	8.0	1.20±0.31	0.01±0.01	−0.001±0.002	0.02±0.01	0.03±0.01	1.13

tions, the observed events, represented by the cross-hatched histograms, were corrected for biases given by the corrections $C(x,y)$ and finally for the radiative corrections. The corrected data are fit by the form $dN(x)/dy = a(x)+b(x)(1-y)^2$ in the intervals shown by the vertical dashed lines. The results of the fits are shown by the solid curves on Fig. 12, and the parameters $a(x)$ and $b(x)$ are given in Table IV.

We emphasize that since we do not know the $\bar{\nu}$ flux, the absolute values of $a(x)$ and $b(x)$ are unknown. Only the x dependence of each and the ratio $a(x)/b(x)$ are determined. The overall normalization, which defines the units of Table IV, is discussed below. We also emphasize that in the fitting, we did not constrain $a(x)$ to be positive so that the curves of Fig. 12 go slightly negative at large y and large x.

Table IV also gives the χ^2 per degree of freedom (χ^2/ND) for each fit. The χ^2/ND is reasonable, which indicates that within our statistical precision, the data are well described by the naive quark-parton model. The overall χ^2/ND is 111/104. The fits were repeated while increasing and decreasing the y range by 0.05 on each side and no significant differences were observed. The fits are also stable against the exact form of the QPM used in the MC program, as well as against the variations in the methods used to calculate the neutrino energy and to select the muon track. We, therefore, use the statistical errors as a measure of the true uncertainties.

A convenient and often used parametrization of the antiquark content of the nucleon is the parameter $B^{\bar{\nu}p}(x)$ defined as

$$B^{\bar{\nu}p}(x)=\frac{xF_3^{\bar{\nu}p}(x)}{F_2^{\bar{\nu}p}(x)} = \frac{b(x)-a(x)}{b(x)+a(x)} . \tag{15}$$

The x variation of this parameter, which is independent of the flux normalization, is also given in Table IV and is shown in Fig. 13. In terms of the quark densities,

$$B^{\bar{\nu}p}(x)=\frac{u(x)-\bar{d}(x)-\bar{s}(x)}{u(x)+\bar{d}(x)+\bar{s}(x)} \tag{16}$$

and so B measures the relative importance of the quark and antiquark contributions to the nucleon. For $x>0.25$, our results for $B^{\bar{\nu}p}(x)$ are consistent

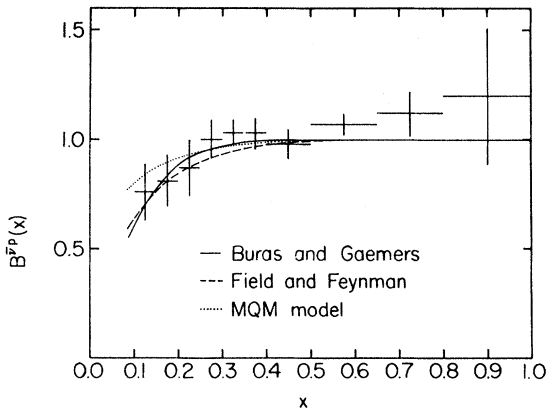

FIG. 13. The x variation of the ratio $B^{\bar{\nu}p}(x) = xF_3^{\bar{\nu}p}(x)/F_2^{\bar{\nu}p}(x)$. The curves show the predictions of the Buras and Gaemers parametrization (solid curve), the Field and Feynman calculation (dashed curve), and the MQM model (dotted curve).

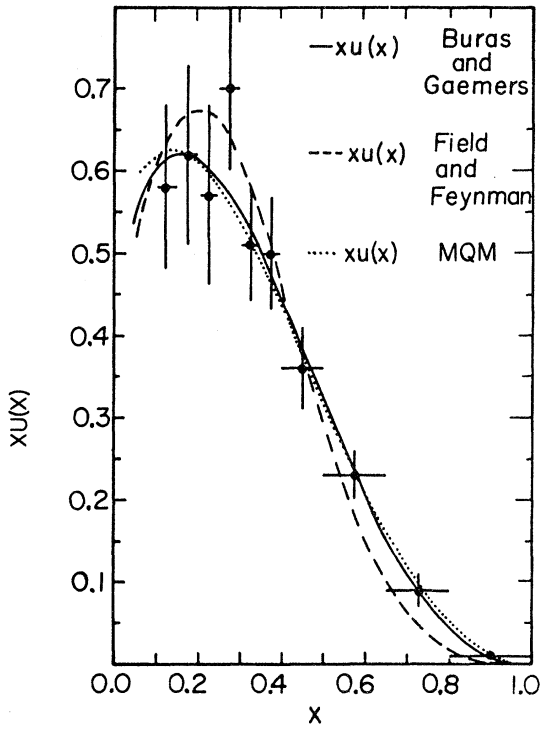

FIG. 14. The up-quark momentum distribution in the proton, $xu(x)$. The data are normalized to the solid curve, which is the prediction of the Buras and Gaemers parametrization at $Q^2=4.5$ (GeV/c)^2. The field and Feynman and MQM parametrizations are also shown in the dashed and dotted curves, respectively.

with unity, which implies no significant antiquark contribution in this region. The curves in Fig. 13 are predictions based on three different parametrizations of the quark densities. The Field and Feynman[18] (FF) prediction is Q^2-independent and was obtained by fitting electroproduction and early neutrino data, as well as by applying a number of theoretical constraints. In the Buras and Gaemers[19] (BG) parametrization, the quark distributions have a Q^2 dependence chosen to satisfy the structure function moment equations predicted by asymptotically free gauge theories. The BG curve on Fig. 13 was calculated using the parameters obtained by the authors from fits to electron and muon scattering data at $Q^2=4.5$ (GeV/c)^2, which is the average Q^2 value of our experiment. Evaluating the BG formulas instead at the average Q^2 appropriate for each x bin has a negligible effect.

The massive-quark model (MQM) of Castorina *et al.*[20] has also been compared to our data. The MQM model, which involves a smaller number of adjustable parameters, has a Q^2 dependence which arises from quark mass effects. It was again evaluated at $Q^2=4.5$ (GeV/c)^2. As can be seen from Fig. 13, all the curves provide a reasonable fit to the data. We evaluated the BG and FF models with a full $\bar{s}$-quark contribution.

Figure 14 shows our result for $xu(x)$. The data are area normalized to the solid curve, which is the prediction from the BG parametrization of the quark densities. The normalization of this curve to the data defines our units. The dashed and dotted curves are the FF and MQM predictions, respectively. Since the integrals $\int_{0.1}^{1} xu(x)dx$ have the values 0.26, 0.24, and 0.30 for the BG, FF, and MQM parametrizations, respectively, the last two predictions have been multiplied by 1.09 and 0.87, respectively, in order to normalize the curves to the data of Fig. 14. As can be seen from the figure, the BG and MQM parametrizations give very similar predictions for the shape of $xu(x)$, which is all that we measure, and are slightly favored by the data over the FF prediction.

Figure 15 shows the antiquark momentum distribution in the proton $x[\bar{d}(x)+\bar{s}(x)]$. The units are fixed by the normalization of $xu(x)$ to the BG prediction. The solid curve is our best fit of the form $A(1-x)^{\alpha}$, where both A and α were left free in the fit. We obtain $A=0.45\pm0.44$ and $\alpha=12.2\pm5.9$, with a $\chi^2/\mathrm{ND}=5/8$. The value of α is independent of the normalization and is consistent with the value $\alpha=11.74$ used in the BG parametrization of the antiquark distributions. Fixing α to the value 11.74, we find $A=0.42\pm0.15$, with χ^2/ND being only slightly worse than in the first fit. With these values of α and A, the quark momentum integral for antidown plus antistrange sea quarks

$$\bar{D}+\bar{S}=\int_0^1 x[\bar{d}(x)+\bar{s}(x)]dx$$

is found to be 0.033 ± 0.012, which may be compared to the FF value of 0.032, the BG value of 0.042, and to the MQM value of 0.020. It should be noted that the contribution of $x\bar{s}(x)$ is only a lower limit to the total $x\bar{s}(x)$ content of the proton since threshold effects[21,22] are likely to be affecting part of our data.

Figure 16 shows the results for $F_2^{\bar{\nu}p}(x)$ and $xF_3^{\bar{\nu}p}(x)$ obtained under the assumption that $2xF_1^{\bar{\nu}p}(x)=F_2^{\bar{\nu}p}(x)$. The solid, dashed, and dotted curves are the BG, FF, and MQM predictions. In Fig. 17 we show our result for $F_2^{\bar{\nu}p}(x)$ (solid circles) compared with the absolute measurements of $F_2^{\nu N}(x)$ obtained by the Big European Bubble

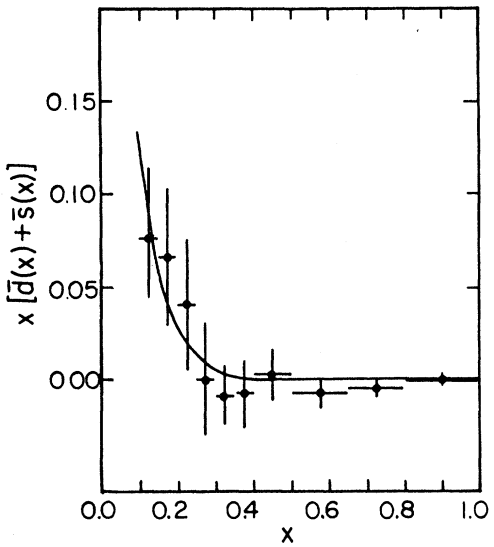

FIG. 15. The antiquark momentum distribution in the proton $x[\bar{d}(x)+\bar{s}(x)]$. The solid curve is the best fit to the form $A(1-x)^{\alpha}$ over the range $0.1 \leq x \leq 1.0$.

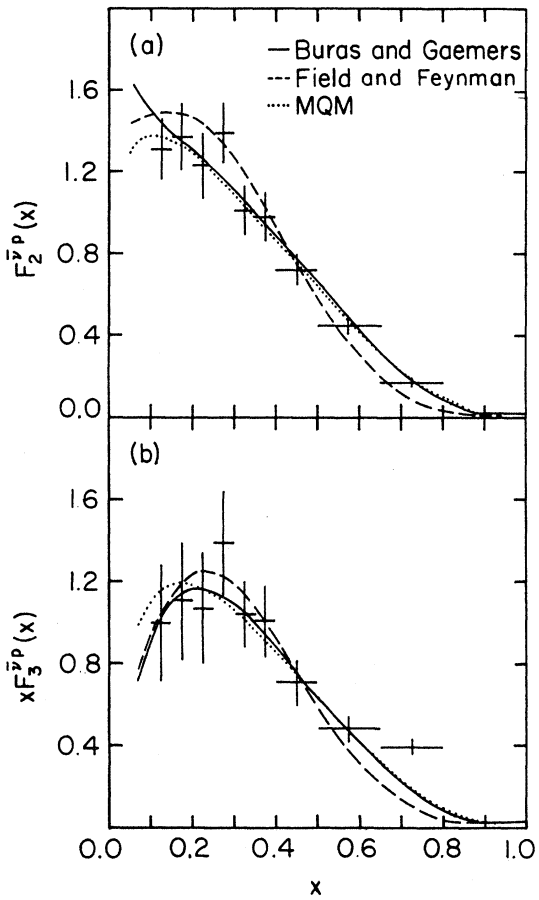

FIG. 16. (a) The x dependence of $F_2^{\bar{\nu}p}(x)$. The curves show the Buras and Gaemers prediction (solid curve), the Field and Feynman prediction (dashed curve), and the MQM prediction (dotted curve), all calculated at $Q^2=4.5$ (GeV/c)^2. (b) The x dependence $xF_3^{\bar{\nu}p}(x)$ compared to the predictions of the three models.

Chamber (BEBC) Collaboration[9] (open squares) and the CERN-Dortmand-Heidelberg-Saclay (CDHS) Collaboration[10] (solid triangles). Since in the latter, the energy of the beam was considerably higher than in our experiment, the CDHS data shown in Fig. 17 are for events with hadronic energy between 5 and 10 GeV. For this selection, the average Q^2 of the CDHS events is similar to ours. The BEBC points were obtained by averaging the data[9] for the Q^2 range from 1 to 30 (GeV/c)^2, a range that is also similar to that in our own experiment. The curves are the BG predictions at $Q^2=4.5$ (GeV/c)^2. Note that the BG parametrization gives a reasonable prediction for $F_2^{\nu N}(x)$.

Any difference in shape between $F_2^{\nu N}(x)$ and $F_2^{\bar{\nu}p}(x)$ for $x>0.3$, where the antiquark contributions is negligible, can be attributed to the difference between the $xu(x)$ and $xd(x)$ quark momentum distributions.

The method that we have employed to extract the structure functions can be applied in different neutrino energy intervals. However, our statistical errors do not allow a sensitive search for scaling violations.

A three-parameter fit to the y distributions at fixed x using Eq. (6) can be used in principle to test the validity of the Callan-Gross relation since the coefficient of $(1-y)$ is proportional to F_2-2xF_1. However, the large correlation between the $1-y$ and $(1-y)^2$ terms makes the method impractical with our data sample. To test for the effects of a possible violation of the Callan-Gross relation, we have made a two-parameter fit to the y distributions using Eq. (6) assuming a constant ratio $2xF_1(x)/F_2(x)=0.82$ independent of x. This value is based on the measurement of the quantity

$$R' = \left[\int 2xF_1(x)dx \Big/ \int F_2(x)dx\right] - 1$$

$$= -0.18 \pm (0.06) \pm (0.04)$$

reported by Benvenuti *et al.*[11] Their result is consistent with values measured in other neutrino,[9] electron,[23] and muon[24] scattering experiments but differs from the CDHS value[10] of -0.03 ± 0.04. When this is carried out, we find that $F_2^{\bar{\nu}p}(x)$ and $xF_3^{\bar{\nu}p}(x)$ decrease uniformly by 3% and 13%,

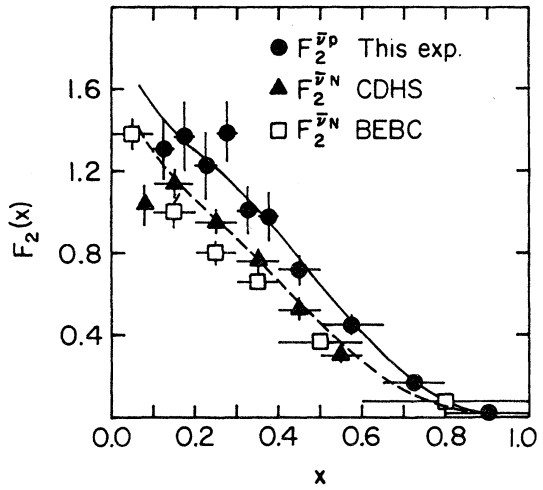

FIG. 17. The x dependence of $F_2^{\bar{\nu}p}(x)$ compared with $F_2^{\nu N}(x)$ measured by the BEBC and CDHS collaborations. The solid and dashed curves show the Buras and Gaemers predictions for $F_2^{\bar{\nu}p}$ and $F_2^{\nu N}$, respectively.

respectively, but with no significant change in the goodness of the fit.

V. CONCLUSIONS

Using a sample of 2275 $\bar{\nu}p \to \mu^+ X^0$ events, we have measured the x dependence of the inelasticity (y) distribution in $\bar{\nu}$ proton scattering. From this measurement we have extracted, assuming the validity of the Callan-Gross relation, the x dependence of the structure functions $F_2^{\bar{\nu}p}(x)$ and $xF_3^{\bar{\nu}p}(x)$ which are then determined up to an overall normalization constant. This is the first measurement of the x dependence of these particular structure functions. We have also measured the ratio $B^{\bar{\nu}p}(x) \equiv xF_3^{\bar{\nu}p}(x)/F_2^{\bar{\nu}p}(x)$, which is independent of the normalization.

The y distributions at fixed x are well described by forms $a+b(1-y)^2$ (with a and b depending only on x) characteristic of the QPM. In the context of this model, we have measured the x dependence of the $xu(x)$ and $x[\bar{d}(x)+\bar{s}(x)]$ quark densities. The result for $xu(x)$ is found to be in excellent agreement with parametrization obtained from fits to electron and neutrino scattering data. Using these parametrizations to fix the $xu(x)$ normalization, we then obtain $x[\bar{d}(x)+\bar{s}(x)]=(0.45\pm0.44)\times(1-x)^{12.2\pm5.9}$. The total fraction of the proton momentum carried by the $\bar{d}$ and $\bar{s}$ antiquarks is found to be

$$\bar{D}+\bar{S}=\int_0^1 x[\bar{d}(x)+\bar{s}(x)]dx = 0.033\pm0.012.$$

ACKNOWLEDGMENTS

This experiment was made possible by the support of the Fermilab Neutrino Department and, in particular, the operating crew of the 15-foot bubble chamber. We also wish to thank our scanners at all three institutions for their careful job. This work was supported by the U. S. Department of Energy.

APPENDIX

In this appendix, we describe the experimental methods used to select the muon track and to calculate the neutrino energy. We also describe the Monte Carlo simulation of the experiment. Finally, we discuss the radiative corrections.

1. Muon selection

In addition to the antineutrino-induced charged-current events

$$\bar{\nu}p \to \mu^+ X^0 , \tag{17}$$

our sample contains charged-current events induced by neutrinos

$$\nu p \to \mu^- X^{++} , \tag{18}$$

as well as $\bar{\nu}$ and ν-induced neutral-current events

$$\bar{\nu}p \to \bar{\nu} X^+ , \tag{19}$$

$$\nu p \to \nu X^+ . \tag{20}$$

Events are assigned to reactions (17) or (18) depending on the sign of the track selected to be the muon or to reactions (19) or (20) if no muon track is selected. We have no way of separating the two neutral-current reactions. Since muon tracks are, in most cases, visually indistinguishable in the bubble chamber from hadronic tracks, we rely on a kinematical method to find the muon. This method gives results of comparable precision to those obtained using the external muon identifier[25] (EMI), and the sample of data so chosen is in good agreement with that resulting from an EMI selection. We have chosen to rely entirely on the

kinematical method due to the greater simplicity of modeling the experiment by a Monte Carlo simulation with this technique.

The kinematical method is based on the fact that the muon track appears, in general, as a single fast particle separated from a clustered jet of hadrons. We distinguish two methods depending on the variable used to separate this particle.

In the first method (momentum-ratio method), the highest-momentum track is selected as the muon if the ratio of its momentum to the momentum of the second fastest track (r) is greater than a set value. If the ratio is less than r, the event is classified as a neutral-current candidate. In Fig. 18, we show, as a series of dots, the parametric variation of the efficiency with the background for different selections of r for the $\bar{\nu}p$ CC events. The dots are plotted at r values differing by 0.2 with $r=2$ marked. As r increases, both the efficiency and the background contamination falls. The results were obtained from a large sample of MC events. The efficiency is defined as the ratio of the number of events with the correct track selected as the μ^+ to the total number of $\bar{\nu}p \to \mu^+ X^0$ events in the sample. The background is then the ratio of the number of events with the wrong track selected as the μ (belonging to any of the reactions 17 to 20) to the total number of events in the selected sample.

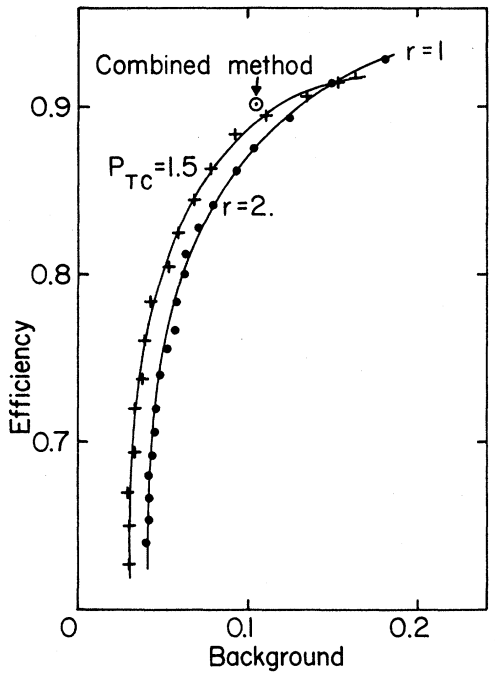

FIG. 18. Parametric variation of the detection efficiency with background for the reaction $\bar{\nu}p \to \mu^+ X$ as calculated from the two different muon selection methods described in the text: the momentum-ratio method (dots) and the transverse-momentum method (plus signs). The parameters r and P_{TC} are incremented by 0.2 for neighboring points. Each parameter decreases as the efficiency and background increase. The final selection which results from the combined method discussed in the text gives a 90% efficiency and a 10% background as shown.

In the second method (maximum-transverse-momentum method or P_{TM} method), the track with the highest transverse momentum (P_{TM}), with respect to the system formed by all the other charged tracks, is selected as the muon if P_{TM} is greater than a certain set value P_{TC}. We again show as the series of plus signs in Fig. 18 the efficiency versus the background using this method. The different plus signs along the curve correspond to values of P_{TC} varying by 0.2 GeV/c with the $P_{TC}=1.5$ GeV/c point marked. Again the efficiency increases as the P_{TC} decreases. The curves on Fig. 18 are hand drawn to connect the points.

In general, the P_{TC} method gives better overall efficiencies for a given background than the ratio method. This is not the case, however, for the subsample of events in which the muon (and therefore the total hadronic system) is produced at small angles with respect to the beam direction. This kinematical region is dominated by events at low x, and for these events, the transverse momentum of the muon, with respect to the total hadronic system, is necessarily small and so few events satisfy the selection $P_{TM} > P_{TC}$.

To define this kinematical region, we use the variable P_{TB} which is the highest transverse momentum of any track in the event with respect to the beam direction. For events with P_{TM} near 1 GeV/c, the two methods give very similar results. As P_{TB} decreases, the ratio method gives better efficiencies for a given background than the P_{TM} method. This can be seen in Fig. 19, where the data have been divided into two subsets defined by having P_{TB} above and below 1 GeV/c. For $P_{TB} > 1.0$ GeV/c, the P_{TC} method is superior to the ratio method and vice versa for the events with $P_{TB} < 1.0$ GeV/c.

It is clear from this difference that a combined method using the momentum ratio method for events with $P_{TB} < 1$ GeV/c and the P_{TM} method for events with $P_{TB} > 1$ GeV/c will give better overall efficiencies for given backgrounds than either of the methods separately. The specific muon selection algorithm that we used is then as follows:

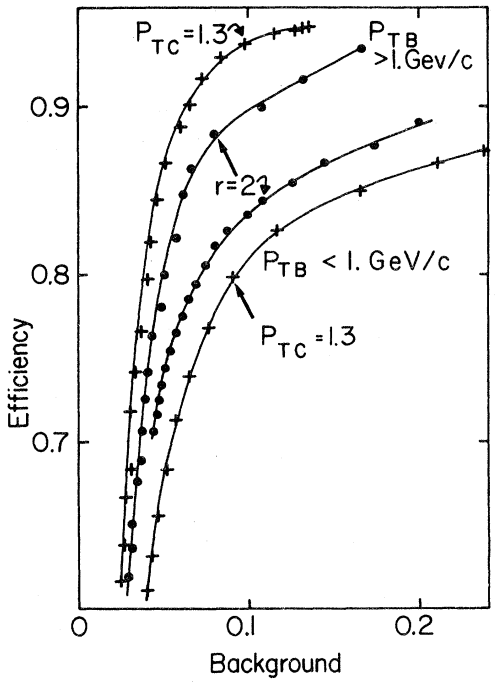

FIG. 19. Detection efficiency versus background for the reaction $\bar{\nu}p \to \mu^+ X$ calculated by the momentum-ratio method (dots) and the transverse-momentum method (crosses). The two sets of points with the highest efficiencies are for events for which the maximum transverse momentum of any track with respect to the beam direction, $P_{TB} > 1$ GeV/c. The two curves with the lower efficiency are for events with $P_{TB} < 1$ GeV/c.

Select the track with the largest P_{TB}. If this value of $P_{TB} > 1$ GeV/c, then find the track with the highest transverse momentum P_{TM} with respect to the system formed by all other charged tracks in the event and call it the muon if $P_{TM} > 1.3$ GeV/c. If this condition is not satisfied but if the maximum P_{TB} of some track in the event is < 1 GeV/c, then find the track with the highest value of r and call it the muon if $r > 2$. The sign of the selected muon track determines if the event ν- or $\bar{\nu}$-induced. If no muon is selected, then the event is classified as a neutral current.

This combined method gives an overall efficiency of 90% and a background of 10% as shown by the point in Fig. 18. In the x,y region selected for analysis, the efficiency is 97% and the background is 7%. This good efficiency and low background is partially a reflection of the dominant $(1-y)^2$ distribution characteristic of $\bar{\nu}$ scattering. The isotropic y distribution of νN scattering would lead to a less favorable situation.

As discussed in the text, the efficiencies and backgrounds, as a function of y for different regions of x obtained using the combined method, are shown in Fig. 5. These curves are the main ingredient in the correction factors described in the text.

2. Energy determination

One of the problems in the study of neutrino interactions in a hydrogen bubble chamber is the poor neutral-particle detection efficiency. Although in general the direction of the neutrino is known (in our case with an accuracy of $\pm 0.07°$), its energy is not, and so events with unseen neutrals are intrinsically underconstrained. The five unknowns are the energy of the neutrino and the components of the neutral system four-momentum. Since there are four conservation equations, there is only one unknown independent variable, and the problem of calculating the neutrino energy reduces to the estimation of this variable. In the method that we have used, called the transverse-mass method, we try to determine an angle α. Figure 20(a) shows the momentum vectors for the reaction $\bar{\nu}p \to \mu^+ h$. The beam is defined to be along the x axis. The hadronic system h breaks up into a charged system of momentum P^c and an unseen neutral system of momentum P^0. The muon and hadronic system h make angles of θ_μ and θ_h, respectively, with respect to the direction of the incident $\bar{\nu}$. As seen in Fig. 20, α is the angle between P^0, the neutral component of the hadronic system, and its projection P_T^0 in the (y,z) plane perpendicular to the beam. The momentum vectors in this transverse plane are shown in Fig. 20(b). In terms of α, the longitudinal momentum of the neutral hadronic system along the beam direction, P_L^0, is given by $P_L^0 = P_T^0 \tan\alpha$ and the neutrino energy E_ν can be written as

$$E_\nu = P_L^\mu + P_L^C + P_T^0 \tan\alpha \ , \tag{21}$$

where P_L^μ and P_L^C are the longitudinal momentum components along the beam direction of the muon and charged hadronic system, respectively.

The determination of α is equivalent to measuring the direction of the total hadronic system. When trying to determine this direction, we can take advantage of the fact that hadrons are produced with limited transverse momentum with respect to the total hadronic momentum. As observed in νp interactions,[26] the distribution of the transverse mass $m_\perp = (P_\perp^2 + m^2)^{1/2}$ (where m is the mass of an individual hadron and $P_\perp$ its transverse momentum with respect to the total hadronic sys-

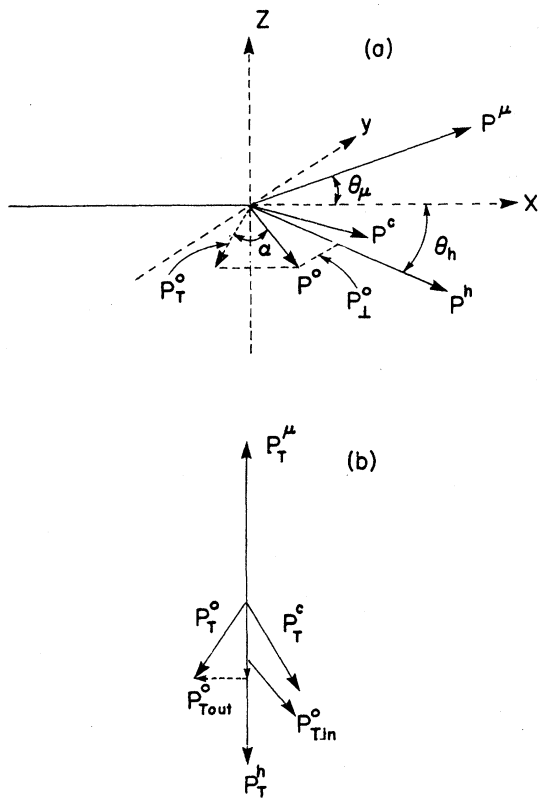

FIG. 20. (a) Momentum vectors of the reaction $\nu p \rightarrow \mu h$. The ν beam is incident along the x axis and the μ and hadronic-system momentum vectors lie in the (x,y) plane. The hadronic system has charged and neutral components of momentum P^c and P^0, respectively. The subscripts L and T refer to longitudinal and transverse components along the x axis, while the subscript $\perp$ refers to components perpendicular to the hadronic direction. The labels in and out refer to components parallel and perpendicular, respectively, to the (x,y) plane. (b) Momentum vectors in the (y,z) plane.

tem) falls off exponentially with $P_\perp$. Then the most probable direction of the total hadronic momentum for a given event is that for which the quantity $\sum_i (P_{\perp i}{}^2+m_i{}^2)^{1/2}$ summed over all the individual hadrons is a minimum. To determine α for a given event, we then form the quantity

$$T(\alpha)=(P_\perp^{0\,2}+\mu_0{}^2)^{1/2}+\sum_{i=1}^{n_c}(P_{\perp i}{}^2+m_i{}^2)^{1/2}\,, \tag{22}$$

where

$$\mu_0{}^2=m_{\pi^0}{}^2+0.01(M_0{}^2-m_{\pi^0}{}^2)\,, \tag{23}$$

and n_c is the number of charged hadrons, M_0 is the effective mass of the neutral-hadronic system, $P_\perp^0$ is the transverse momentum of this system with respect to the direction of the total hadronic system and m_{π^0} is the π^0 mass.

For a given event, $T(\alpha)$ is a single-valued function of α which goes through a minimum. We take as a solution the value of α at this minimum, α_s. Note that for a given value of α, the transverse momentum of the individual neutral hadrons with respect to the total hadronic system is not known (only the transverse momentum of the neutral system is known) and, therefore, their contribution to $T(\alpha)$ appears as a single term. The reason for using μ_0 in this term is described below.

The assumption that the distribution of $(P_\perp{}^2+m^2)^{1/2}$ decreases exponentially can be verified in our data independently of the energy calculation. Although we do not measure $P_\perp$ even for the charged tracks since we do not know the direction of the total hadronic system, we do measure the perpendicular component of $P_\perp$ with respect to the $\nu-\mu-$total-hadron plane, which is the x,z plane in Fig. 20. We call this quantity $P_{\perp\,\text{out}}$. Since the individual hadrons are produced isotropically around the total-hadron direction, the distribution in $P_{\perp\,\text{out}}$ is the same as $P_\perp$ and $\langle P_{\perp\,\text{out}}{}^2\rangle=\frac{1}{2}\langle P_\perp{}^2\rangle$. Figure 21 shows the distribution in the quantity $(P_{\perp\,\text{out}}{}^2+m^2)^{1/2}$ for the hadrons from the events in our sample. An approximate exponential falloff is seen except in the first bin.

Events with no neutral particles should, in principle, have $P_T^0=0$ and therefore, in this case, the neutrino energy will be independent of α. In practice P_T^0, which is obtained as shown in Fig. 20(b) by balancing the momentum of the muon and of the charged hadronic system in the plane perpendicular to the beam direction, is not zero because of resolution effects. A study of the MC-generated events shows that, although α_s is small for events with no neutrals, the energy resolution is better if no correction is made to the visible energy measurement. To separate the sample of events with no neutrals, we use the two components of P_T^0, $P_{T\,\text{in}}^0$, and $P_{T\,\text{out}}^0$, where $P_T^0=(P_{T\,\text{in}}^{0\,2}+P_{T\,\text{out}}^{0\,2})^{1/2}$, and the subscripts in and out refer to components parallel to and perpendicular to the (x,y) plane, respectively. Figure 22 shows a scatter plot of $P_{T\,\text{in}}^0$ versus $P_{T\,\text{out}}^0$ for the real events in the region in which these two quantities are both small. An accumulation of events near the origin is apparent although the distribution of P_T^0 shows no clear peak near zero. Based on a similar plot for MC-

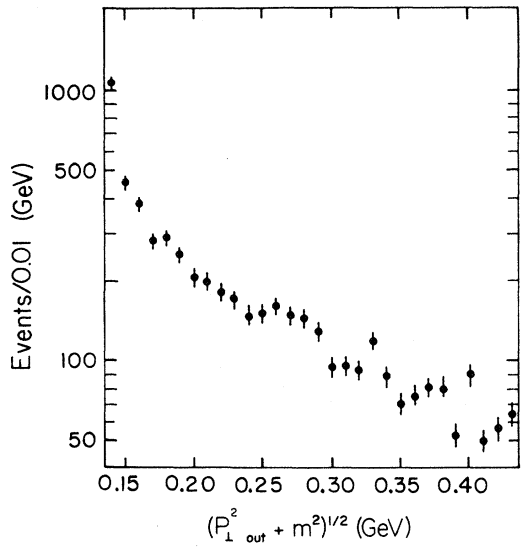

FIG. 21. The distribution in the quantity $(P^2_{\perp\text{out}}+m^2)^{1/2}$ for a sample of tracks from the real events.

generated events, we classify an event as one with no neutrals if $P^0_{T\text{in}}P^0_{T\text{out}}<0.0025$ (GeV/c)^2. This is the region below the curve in Fig. 22.

For events that do have neutral particles, one can obtain a lower limit to the longitudinal momentum of the neutral system along the beam direction P^0_L (and therefore α) by requiring that the effective mass of the neutral hadronic system M_0 is at least equal to a π^0 mass. As a function of M_0, P^0_L is given by

$$P^0_L=\frac{M_0{}^2+P^0_T-D^2}{2D}\,, \tag{24}$$

where

$$D=(P^\mu_L+P^C_L)+m_p-(E^\mu+E^C)\,, \tag{25}$$

and m_p is the proton mass and E^C is the energy of the charged hadronic system. This energy is in general underestimated due to the misidentification of protons and kaons as pions. Now $P^0_{L\,\text{min}}$ is given by Eq. (24) with M_0 equal to the π^0 mass and $\alpha_{\text{min}}=\arctan\,(P^0_{L\,\text{min}}/P^0_T)$.

If α_s is close to 90°, the error in the estimation of E_ν may be large since $dE_\nu/d\alpha$ goes to infinity as α approaches 90°. Based again on MC studies, we put a ceiling in P^0_L for the events with $dE/d\alpha$ greater than 100. This ceiling is (in GeV/c units) $P^0_L=5P^0_T$ if $P^0_T<0.5$ and $P^0_L=10(P^0_T-0.5)+2.5$ if $P^0_T>0.5$. Only 9% of the real events fall into this category.

Figure 23 shows the distribution of the quantity $\Delta E/E=(E_{\text{generated}}-E_{\text{calculated}})/E_{\text{generated}}$ for a sample of MC events using the transverse-mass method to calculate the ν energy. The momentum resolution effects were incorporated into the MC

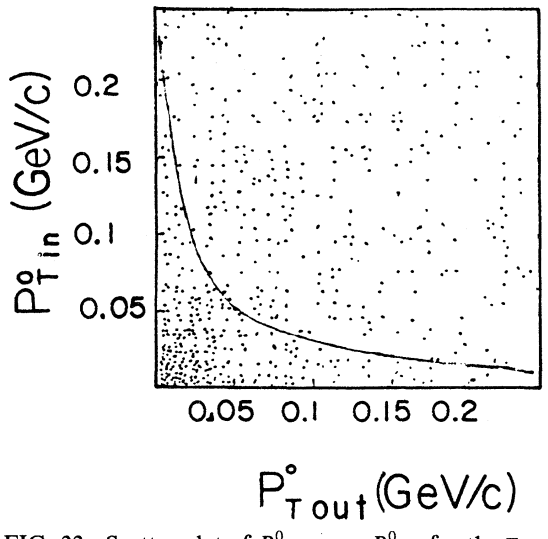

FIG. 22. Scatter plot of $P^0_{t\text{in}}$ versus $P^0_{T\text{out}}$ for the $\bar{\nu}p$ charged-current events, with $P^0_{T\text{in}}$ and $P^0_{T\text{out}}$ both below 0.25 GeV/c. The curve is the equation $P^0_{T\text{in}}\,P^0_{T\text{out}}=0.0025$ (GeV/c)^2.

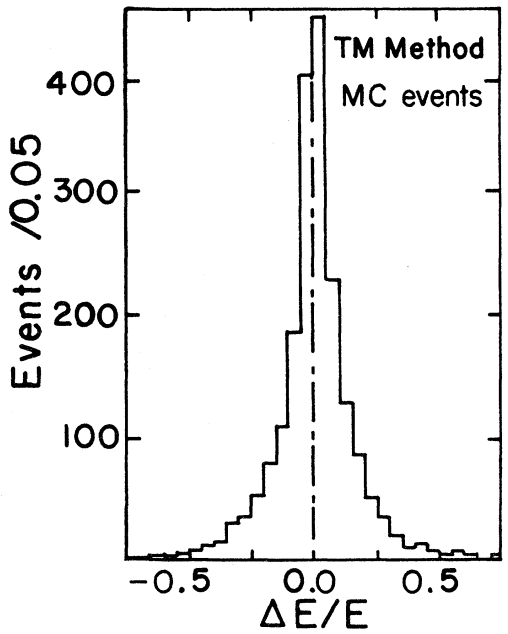

FIG. 23. The distribution of the quantity $\Delta E/E$ for a sample of Monte Carlo events. The calculated energy was obtained using the transverse-mass method.

program. The distribution is symmetric about zero. Forty-three percent of the events have $|\Delta E|/E < 0.05$ while 11% have $|\Delta E|/E > 0.25$; the full width at half maximum is 0.12.

Figure 24 shows the distribution in the variable z for a sample of real events, also obtained using the transverse-mass method to calculate the neutrino energy. The variable z is the transverse momentum of the neutral hadronic system with respect to the total hadronic direction in the ν-μ-total hadron plane ($P^0_{\perp in}$ in our notation); its value for a particular event is related to the neutrino energy.[27] Since the neutral system is produced with azimuthal symmetry with respect to the total hadron direction, the distribution of z should be symmetric about zero and be similar to the distribution of $P^0_{\perp out}$. In the transverse-mass method, we find that the symmetry of the z distribution depends on the way the mass of the neutral hadronic system is incorporated into Eq. (22). The form of μ_0, given in Eq. (23), was used to maximize this symmetry. Figure 25 shows the distribution of $P^0_{\perp out}$ for the same sample of real events. Unlike z, $P^0_{\perp out}$ is measured by balancing the momentum of the charged hadronic system with respect to the ν-μ-total hadron plane. As seen in Figs. 24 and 25, the measured distribution in z is slightly narrower than the distribution of $P^0_{\perp out}$.

The several different methods that have been used in the past to determine the neutrino energy were reviewed in our previous publication.[16] The present method was developed to give the best energy measurement as measured both by the central value and the symmetry of the distribution. Specifically, we find that our transverse-mass method gives 7% more of the events within 5% of the correct energy than does the Grant method.[27] The $\Delta E/E$ distributions are also somewhat more symmetric.

Finally, in Fig. 26, we show the final energy distributions of the $\bar{\nu}p$ and νp charged-current events in our sample that result from our energy selection procedures. The curves are fits to polynomial expansions.

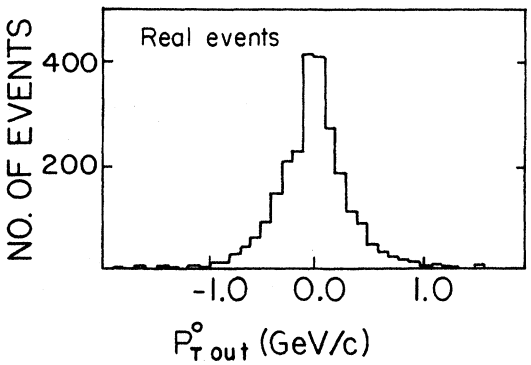

FIG. 25. The distribution in the quantity $P^0_{\perp out}$ for the same sample of events as shown in Fig. 24.

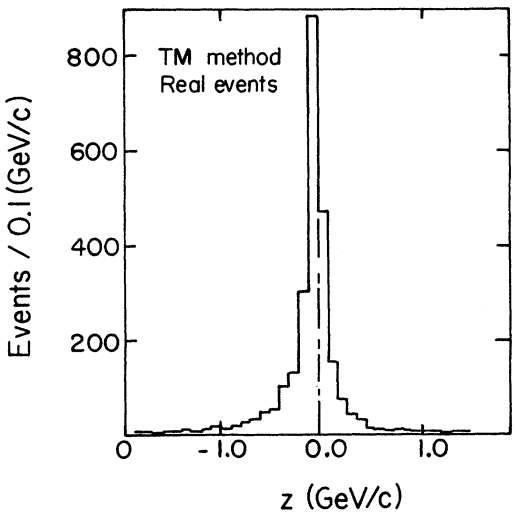

FIG. 24. The distribution in the variable z, described in the text, for a sample of real events using the transverse-mass method to calculate the energy.

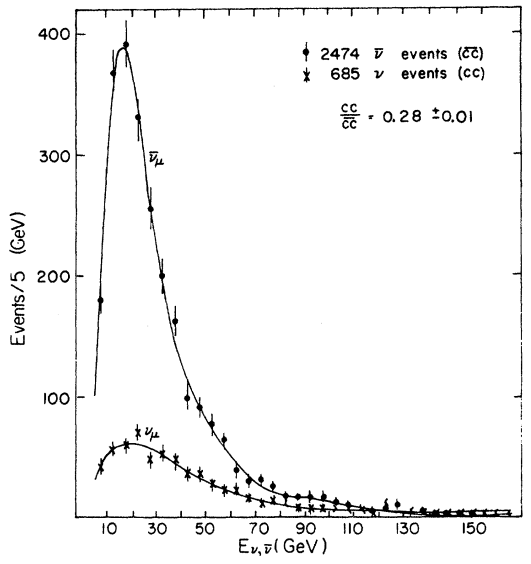

FIG. 26. Calculated energy distributions for the νp and $\bar{\nu}p$ charged-current events. The curves are fits to a polynomial expansion.

3. The Monte Carlo program

In order to correct biases in the data resulting from our methods of selecting the muon and calculating the neutrino energy, as well as from cuts and resolution effects, we simulated the experiment using a Monte Carlo program. The MC events are then passed through the analysis chain in the same manner as the data and the corrections determined by the comparison of the calculated and generated MC distributions.

A flow diagram of the MC program is shown in Fig. 27. The events are generated as charged-current $\bar{\nu}$-induced ($\overline{\mathrm{CC}}$), neutral current $\bar{\nu}$-induced ($\overline{\mathrm{NC}}$), charged-current ν-induced (CC), and neutral current ν-induced (NC) with relative probabilities of 0.59, 0.18, 0.16, and 0.07. The ratios, $\overline{\mathrm{NC}}/\overline{\mathrm{CC}}$ of 0.31 for $\bar{\nu}p$ and NC/CC of 0.43 for νp are from the QPM predictions with $\sin^2\theta_W=0.25$ and the Field and Feynam parametrization of the parton densities. The ratio $\mathrm{CC}/\overline{\mathrm{CC}}$ of 0.28 is obtained from the number of observed ν- and $\bar{\nu}$-induced events, using the iterative procedure outlined below.

An energy for each event is then generated, distributed as in the corresponding ν or $\bar{\nu}$ curve of Fig. 28. To obtain these curves, which are the input energy spectra and which determine the ratio $\mathrm{CC}/\overline{\mathrm{CC}}$, we start with the observed energy distributions of the real events shown in Fig. 26. The correction factors, calculated by using the data of Fig. 26 as input, are applied with the opposite sign to the MC data and result in the curves of Fig. 28. Now subjecting this MC data to the selection procedures gives the distributions shown in Fig. 29. The curves in this figure are the same as those of Fig. 26. As can be seen, the agreement is good. The differences between Figs. 28 and 29 is a measure of how the muon-selection and energy-calculation procedures affect the energy spectra.

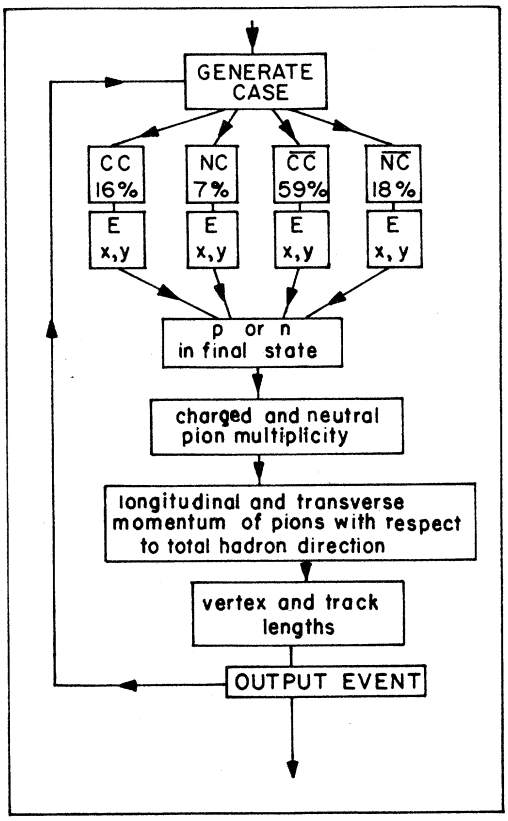

FIG. 27. Flow diagram of the MC program.

The distributions in the scaling variables x and y are generated according to the QPM cross sections

$$\frac{d\sigma^{\overline{\mathrm{CC}}}}{dx\,dy}=\frac{G^2ME_\nu}{\pi}2x[\bar{d}(x)+\bar{s}(x)+(1-y)^2u(x)]\,, \tag{26}$$

$$\frac{d\sigma^{\mathrm{CC}}}{dx\,dy}=\frac{G^2ME_\nu}{\pi}2x[d(x)+s(x)+(1-y)^2\bar{u}(x)]\,, \tag{27}$$

$$\frac{d\sigma^{\overline{\mathrm{NC}}}}{dx\,dy}=\frac{G^2ME_\nu}{\pi}2x\{[a^2(1-y)^2+c^2]u(x)+[b^2(1-y)^2+d^2][d(x)+s(x)]$$
$$+[a^2+c^2(1-y)^2]\bar{u}(x)+[b^2+d^2(1-y)^2][\bar{d}(x)+\bar{s}(x)]\}\,, \tag{28}$$

$$\frac{d\sigma^{\mathrm{NC}}}{dx\,dy}=\frac{G^2ME_\nu}{\pi}2x\{[a^2+c^2(1-y)^2]u(x)+[b^2+d^2(1-y)^2][d(x)+s(x)]$$
$$+[a^2(1-y)^2+c^2]\bar{u}(x)+[b^2(1-y)^2+d^2][\bar{d}(x)+\bar{s}(x)]\}\,, \tag{29}$$

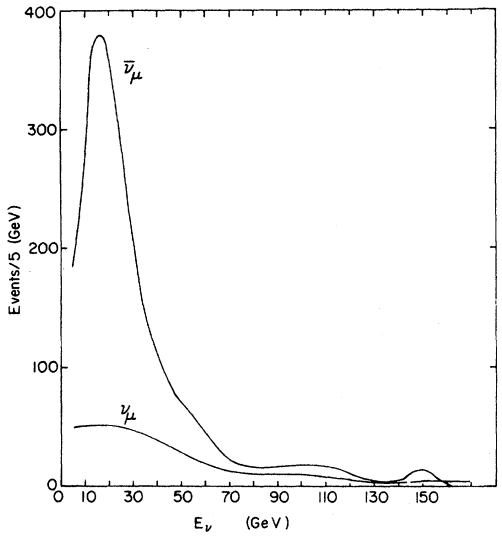

FIG. 28. Energy distribution for νp and $\bar{\nu} p$ events used as input to the MC program.

where

$$a = \tfrac{1}{2} - \tfrac{2}{3}\sin^2\theta_W \ , \tag{30}$$

$$b = -\tfrac{1}{2} + \tfrac{1}{3}\sin^2\theta_W \ , \tag{31}$$

$$c = -\tfrac{2}{3}\sin^2\theta_W \ , \tag{32}$$

and

$$d = \tfrac{1}{3}\sin^2\theta_W \ . \tag{33}$$

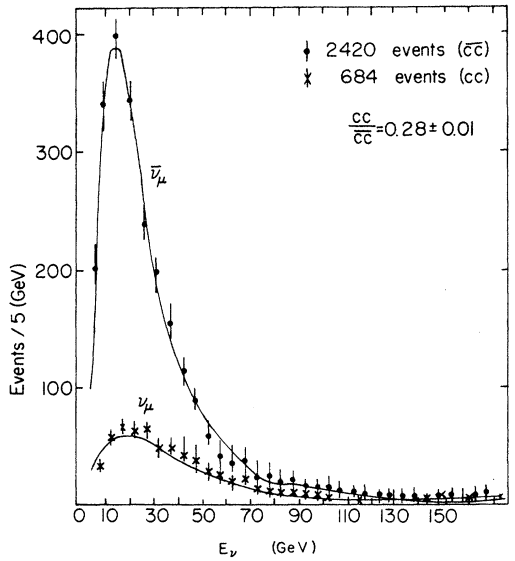

FIG. 29. The energy distribution for ν and $\bar{\nu}$ MC-generated charged-current events after subjecting the events to the selection procedures. The curves are the fits to the energy distributions for the real events shown in Fig. 26.

We use the Field and Feynman parametrization of the parton densities $u(x)$, $d(x)$, $s(x)$, $\bar{u}(x)$, $\bar{d}(x)$, $\bar{s}(x)$, and $\sin^2\theta_W = 0.25$. The beam fluxes shown in Fig. 2 result from the use of these cross sections together with the event distributions of Fig. 29.

The breakup of the system at the hadronic vertex is accomplished in several steps.

(i) The properties of the hadronic system are assumed to depend only on the hadronic mass W, where $W^2 = M^2 + 2MExy(1/x - 1)$.

(ii) One of the final-state hadrons is assigned to be a proton or a neutron with equal probability independent of W.

(iii) The remaining final-state hadrons are assumed to be pions. The pion multiplicity is generated as a Poisson distribution in the total number of pions. The average multiplicity is assumed to vary with W. According to our measurements,[15] $\langle n_c^H \rangle = (0.06 \pm 0.06) + (1.22 \pm 0.33) \ln W^2$, where n_c^H is the number of charged hadrons. The mean neutral-pion multiplicity $\langle n_0 \rangle$ varies with the charged-hadron multiplicity as $\langle n_0 \rangle = (0.57 \pm 0.19) + (0.37 \pm 0.07) n_-$, where n_- is the number of negative hadrons.

(iv) The longitudinal and transverse momenta of all the hadrons with respect to the direction of the total hadronic system are generated with azimuthal symmetry and an exponential transverse-momentum dependence of $\exp(-5.6 P_\perp^2)$. The longitudinal momentum is taken to vary as $\exp(-P_{||})$. Energy and momentum conservation are imposed in the rest frame of the hadronic system. In this system, the average momentum in a given direction is subtracted from the momenta of all the individual particles in that direction. This assures momentum conservation. To assure energy conservation, all the momenta along the hadronic direction $P_{||i}$ are scaled by a factor f so as to satisfy the equation

$$\sum_i [(f P_{||i})^2 + (P_{\perp i}^2 + m_i^2)]^{1/2} = W \ , \tag{34}$$

where the sum extends to all the hadrons.

(v) To simulate the resolution effects, a track length is generated for each charged particle. This is accomplished by generating a vertex for the event radomly distributed inside the fiducial volume and then "swimming" each track in the chamber magnetic field folding in the dE/dx energy loss due to ionization as well as interaction, decay, and stopping probabilities. To smear the track momentum, the measuring error contribution was assumed to come from a sagitta error distri-

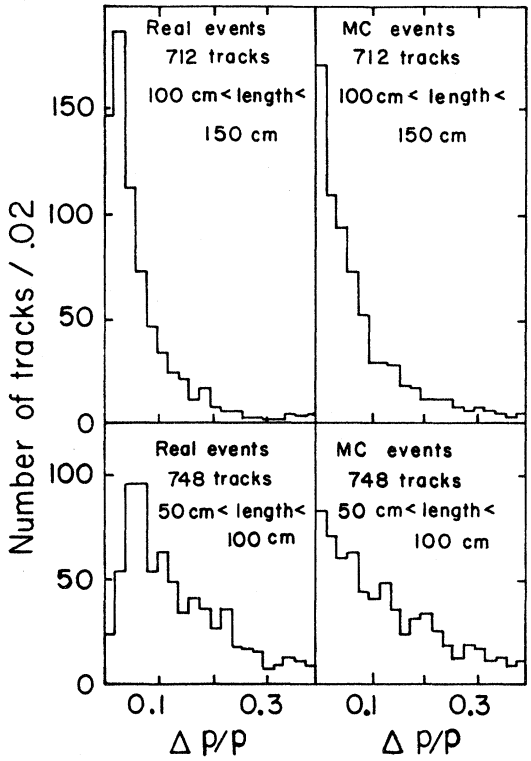

FIG. 30. The $\Delta p/p$ distribution of real and MC tracks for two different length intervals.

buted about zero with a full width at half maximum of 900 μm. This number is chosen to obtain similar $\Delta p/p$ distributions for MC tracks and real tracks as a function of measured length. These distributions are shown in Fig. 30 for two typical length intervals. As can be seen, there is reasonable agreement between the MC and the real tracks. The effect of the smearing on the correction factors is small.

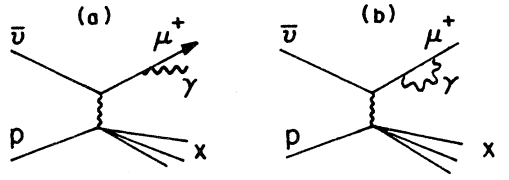

FIG. 31. Diagrams of the processes contributing to the lepton logarithmic radiative corrections.

4. Radiative corrections

Radiative corrections to the inclusive deep-inelastic ν and $\bar{\nu}$ cross sections could be important in the study of antiquark distributions since the antiquark content of the nucleon is small. However, for our experiment, the effects of the radiative corrections are much smaller than the statistical errors.

The radiative correction to νp scattering have been studied by a number of authors.[17,28,29] Here we follow the treatment of de Rújula *et al.*[17] in which only lepton leading-logarithmic corrections are considered. The corrections arise from the collinear emission and reabsorption of photons by the muon as shown in Fig. 31. The effect, which is to reduce the energy of the muon at a fixed angle, causes the event to migrate from smaller to larger y. Thus the observed cross section $d\sigma_0/dy$, will be overestimated at large y and underestimated at small y, the effect being more pronounced at small x. Quantitatively, the relation between the observed (uncorrected) cross section σ_0 and the bare (corrected) cross section σ_B is given by

$$\frac{d\sigma_0}{dx\,dy}=\frac{d\sigma_B}{dx\,dy}+\frac{\alpha}{2\pi}\ln\left[\frac{s(1-y+xy)^2}{\mu^2}\right]\int_0^1 dz\,\frac{1+z^2}{1-z}\left[\frac{y\theta(z-z_{\min})}{z(y+z-1)}\frac{d\sigma_B}{dx\,dy}\bigg|_{\substack{x=\tilde{x}\\y=\tilde{y}}}-\frac{d\sigma_B}{dx\,dy}\right], \tag{35}$$

where

$$s\approx M_p{}^2+2M_pE_\nu,\quad z_{\min}=1-y+xy,$$

$$\tilde{x}=\frac{xy}{z+y-1},\text{and }\tilde{y}=\frac{z+y-1}{z}.$$

To evaluate the integral in Eq. (35), one can use the observed cross section under the integral sign or alternatively, one can use a model for $d\sigma_B/dx\,dy$. We have used the QPM cross section with the quark densities given by the Buras and Gaemers parametrization at $Q^2=4.5$ (GeV/c)^2. To take into account charm threshold effects, we give a 50% relative weight to the $\bar{s}$ contribution. The radiative corrections are then given by $1/[1+\Delta(x,y,E)]$, where

$$\Delta(x,y,E)=\left[\frac{d\sigma_0}{dx\,dy}-\frac{d\sigma_B}{dx\,dy}\right]\Big/\frac{d\sigma_B}{dx\,dy}\ . \quad (36)$$

The function Δ is shown in Fig. 9 as a function of y for different x values at an energy of $E=25$ GeV.

We have investigated the sensitivity of the radiative corrections to the exact form of the quark densities and find the dependence to be minimal.

---

*Present address: Argonne National Laboratory, Argonne, IL 60439.
†Present address: CERN, EP Division, Geneva 23, Switzerland.
‡Present address: Bell Telephone Laboratories, Naperville, IL 60540.
§Present address: U.S. Department of Energy, Washington, D.C. 20545.
||Present address: Fermi National Accelerator Laboratory, Batavia, IL 60510.
¶Present address: Department of Physics, University of Toronto, Ontario, M5S 1A7, Canada.
**Present adress: Lawrence Livermore Laboratory, University of California, Livermore, CA 94550.

[1]R. P. Feynman, *Photon Hadron Interactions* (Benjamin, New York, 1971).
[2]G. Miller *et al.*, Phys. Rev. D 5, 528 (1972).
[3]T. Eichten *et al.*, Phys. Lett. 46B, 274 (1973).
[4]J. D. Bjorken, Phys. Rev. 197, 1547 (1969).
[5]S. J. Barish *et al.*, Phys. Lett. 66B, 291 (1977).
[6]C. G. Callan and D. G. Gross, Phys. Rev. Lett. 22, 156 (1969).
[7]E. Fernandez *et al.*, Phys. Rev. Lett. 43, 1975 (1979).
[8]H. Deden *et al.*, Nucl. Phys. B85, 269 (1975).
[9]P. C. Bosetti *et al.*, Nucl. Phys. B142, 1 (1978).
[10]J. G. H. deGroot *et al.*, Z. Phys. C 1, 143 (1979).
[11]A. Benvenuti *et al.*, Phys. Rev. Lett. 42, 1317 (1979).
[12]W. S. C. Williams, in *Proceedings of the 1979 International Symposium on Lepton and Photon Interactions at High Energies, Fermilab,* edited by T. B. W. Kirk and H. D. I. Abarbanel (Fermilab, Batavia, Illinois, 1980), p. 384.
[13]R. J. Stefanski and H. B. White Jr., Fermilab Report No. FN292, 2060.000, 1976 (unpublished).
[14]C. L. Wang, Phys. Rev. D 10, 3876 (1974).
[15]M. Derrick *et al.*, Phys. Rev. D 18, 7 (1978).
[16]S. J. Barish *et al.*, Phys. Rev. D 18, 2205 (1978).
[17]A. de Rújula *et al.*, Nucl. Phys. B154, 394 (1979).
[18]R. D. Field and R. P. Feynman, Phys. Rev. D 15, 2590 (1977).
[19]A. J. Buras and K. J. F. Gaemers, Nucl. Phys. B132, 249 (1979).
[20]P. Castorina, G. Nardulli, and G. Preparata, Nucl. Phys. B163, 333 (1980).
[21]R. Brock, Phys. Rev. Lett. 44, 1027 (1980).
[22]S. J. Barish *et al.*, Phys. Rev. Lett. 45, 783 (1980).
[23]M. Mestayer, SLAC Report No. 214, 1978 (unpublished).
[24]B. A. Gordon *et al.*, Phys. Rev. Lett. 41, 615 (1978).
[25]R. J. Cence *et al.*, Nucl. Instrum. Methods 138, 245 (1976).
[26]J. Bell *et al.*, Phys. Rev. D 19, 1 (1979).
[27]A. Grant, Nucl. Instrum. Methods 127, 355 (1975).
[28]J. Kiskis, Phys. Rev. D 8, 2129 (1973).
[29]R. Barlow and S. Wolfram, Phys. Rev. D 20, 2198 (1979).